ELSEVIER

Contents lists available at ScienceDirect

Corrosion Science

journal homepage: www.elsevier.com/locate/corsci





Corrosion behavior of a bulk nanocrystalline Al-Fe alloy

F. Ozdemir ^{a, b}, C.S. Witharamage ^a, J. Christudasjustus ^a, AA. Darwish ^a, H. Okuyucu ^b, R. K. Gupta ^{a, *}

- ^a Department of Materials Science and Engineering, North Carolina State University, Raleigh, NC 27695, USA
- ^b Department of Materials Engineering, Ankara Yildirim Beyazit University, Ankara, Türkiye

ARTICLE INFO

Keywords: Aluminum alloys Nanocrystalline alloys Corrosion High-energy ball milling Al-Fe alloy Microstructure

ABSTRACT

Nanocrystalline Al-Fe alloy, with uniform microstructure and high solid solubility of Fe, has been produced by high-energy ball milling. Cyclic potentiodynamic polarization tests revealed high pitting potential. Hardness and corrosion resistance of the Al-Fe alloy were higher than any commercial Al alloy. High hardness and corrosion resistance were attributed to the nanocrystalline structure and formation of solid solution. X-ray photoelectron spectroscopy, secondary ion mass spectrometry, and scanning transmission electron microscopy indicated the incorporation of Fe to the surface film and Fe enrichment at the alloy/surface film interface, which were attributed to the enhanced corrosion performance.

1. Introduction

The increasing demand for high-strength and lightweight alloys has led to the development of a wide variety of aluminum alloys. Iron (Fe) is generally undesirable and the most common impurity in aluminum alloys [1], which forms secondary phases due to extremely low solid solubility- a maximum of ~0.025 at% at 655 °C [2]. However, Al alloys with high iron content could be auspicious considering the low cost of Fe and efforts being made to remove Fe from Al. Few studies has been reported to introduce the Fe to Al to enhance the high temperature performance owing to the high melting temperature of Al-Fe intermetallics and low diffusion coefficient of Fe in Al [3,4]. However, these brittle Al-Fe intermetallics have significantly limited the plastic deformation and reported to decrease fracture toughness [5] and deteriorated corrosion resistance due to galvanic interactions with the Al matrix [6]. Therefore, exploring new techniques that reverse the deleterious effects of iron in aluminum while preserving the benefits of it is of great merit.

Various techniques, including rapid solidification [7], additive manufacturing [8,9], and severe plastic deformation techniques [5, 10–14], have been proposed to synthesize Al-Fe alloys with modified microstructures. High-energy ball milling (HEBM) is a proven technique for homogenizing the microstructure by uniform dispersion of constituent particles and increased solid solubility of alloying elements [15]. The vast majority of the studies on high-energy ball milled Al-Fe alloys investigated the microstructure and mechanical properties. Sasaki et al.

reported the significant grain refinement in mechanically alloyed Al-5at %Fe alloys whose matrix consists of refined intermetallic constituents such as Al_6Fe and $Al_{13}Fe_4$ [10,16]. The alloys are reported to have compressive strengths exceeding 1 GPa with high ductility. Nayak et al. reported the increasing hardness with increasing Fe content in Al-Fe alloys due to formation of $Al_{13}Fe_4$, a large number of defects during the alloying process, and absence of soft Al phase [11]. Mukhopadhyay et al. reported the dissolution of 4.5 at% Fe in Al matrix by mechanical alloying for 20 h [5]. It should be noted that solid solubility of Fe in Al at room temperature is negligible.

Aluminum alloys, unlike pure aluminum, exhibit poor corrosion resistance due to the micro galvanic interaction of heterogeneities in the microstructure, which leads to the breakdown of the protective passive film and promotes localized corrosion [17]. Iron has an extremely detrimental effect on corrosion because it is present in the form of cathodic constituents such as Al₃Fe, [6]. In addition, iron may also be present in the form of more detrimental compounds such as AlCuFeSi, Al₇Cu₂Fe, AlCuFeMn, AlFeMnSi in the high-strength aluminum alloys [18–22]. Since the corrosion of aluminum alloys strongly depends on their microstructure, nanocrystalline alloys are expected to have different corrosion properties due to their refined microstructure. Mechanical alloying is a promising method for the formation of nanocrystalline alloys, among the techniques that can provide modified structures and thus aid in a significant enhancement in corrosion resistance [15,23]. Recent studies on nanocrystalline Al alloys produced by

E-mail address: rkgupta2@ncsu.edu (R.K. Gupta).

 $^{^{\}ast}$ Corresponding author.

high-energy ball milling have demonstrated the possibility of simultaneous improvement in strength and corrosion [24–29], where Al-Cr [30, 31], Al-V [32], Al-Mo, Al-Nb, Al-Mn, Al-Ti, Al-Si [26,27] alloys prepared by high-energy ball milling exhibited enhanced strength and corrosion performance than commercial Al alloys. Additionally, the corrosion performance was attributed to the improved solid solubility of the corrosion-resistant elements within the Al matrix, which provided solute enrichment at the metal/film interface, increased propensity for re-passivation, release of corrosion-inhibiting compounds, and increased vacancy annihilation in the passive film [23,32,33].

The abovementioned literature reports the presence of iron and ironcontaining intermetallics in the high-energy ball milled aluminum alloys. The source of iron in these works is attributed to either iron impurities in the material or possible contamination from hardened stainless-steel milling media [15,27,34-36]. However, understanding the role of the Fe contamination on the microstructure and corrosion characteristics of ball milled alloys attracted limited attention. Moreover, iron restricts the widespread use of aluminum alloys, especially in recycled aluminum, where the iron content accumulates after each recycling step. It has been shown that the detrimental effects of iron could be reduced by controlling the intermetallics. For example, fast solidification rates in Al-Fe alloys have resulted in high corrosion resistance [7]. Therefore, understanding the corrosion, microstructure, and mechanical properties of ball milled Al-Fe alloys is of great importance for the development of new Al alloys, reducing cost, and improving recyclability, since recycling of the Al is considered critical for sustainability [37,38].

The corrosion and strength of a nanocrystalline Al-Fe alloy have been investigated in this study. The role of iron as an alloying element in the high-energy ball milled Al-5at%Fe alloys was investigated in terms of corrosion and strength and compared with pure Al and Al-5at%M alloys (M: Si, Cr, Ti, Mn, Ni, Mo, V, Nb) prepared with the same experimental parameters reported in the literature [27]. The role of microstructure and passive film was investigated and discussed to evaluate the mechanisms and effectiveness of iron in improving the corrosion resistance and strength of the Al-5at%Fe alloy.

2. Experimental

F. Ozdemir et al.

2.1. Alloy production

Al-5at%Fe alloy powder was mechanically alloyed in a Fritsch Pulverisette 5 ball mill. Gas atomized aluminum powder (99.7% purity) and iron powder (5 at%) were weighed in a high purity argon atmosphere within a glovebox. The powder mixture was placed in hardened stainless-steel containers and sealed inside the glovebox along with the following elements; Stainless-steel balls with a diameter of 10 mm and a ball to powder weight ratio of 16:1, 1.5 wt% stearic acid as a process controlling agent (PCA). Mechanical alloying was conducted for 100 h at a rotation speed of 280 rpm. Ball milling process was programmed with a one hour pause after each hour of milling operation to eliminate problems due to overheating. The milling status was examined to check the powder structure in the glovebox after every quartet of the milling operation. The milled Al-5at%Fe powder was then consolidated into the 7 mm diameter pellets with 3 mm thickness through compaction at laboratory ambient temperature. 3 GPa of single-ended pressure was applied for 10 min on each specimen. The cold compacted cylindrical pellets are referred to as Al-5Fe and Al pellets, 3-12 mm in diameter (Sigma-Aldrich, 338788, 99.99% purity) are referred to as Pure Al in this manuscript.

2.2. Characterization

The Scanning Electron Microscopy (SEM) was performed in a FEI Verios 460 L field emission SEM equipped with an Oxford energy dispersive X-ray spectrometer with an electron landing energy of 20 kV.

Specimens for Transmission Electron Microscopy (TEM) investigation were prepared in a ThermoFisher Quanta 3D FEG, a Focused Ion Beam and Scanning Electron Dual- beam Microscope (FIB-SEM). Specimens were protected with a platinum coating to avoid surface damage from ion implantation and irradiation. A landing voltage of 30 kV with various beam currents was utilized to monitor the specimen. Crosssection lift-out with an approximate thickness of 1-2 µm of lamella was performed by an omniprobe manipulator. Further thinning and contamination cleaning were carried out after placing the lamella on a TEM grid. TEM specimens were stored under vacuum after final polishing until TEM investigation in a Thermofisher Talos F200X Field Emission Gun Scanning Transmission Electron Microscope (S/TEM) operated at 200 kV. X-Ray Diffraction (XRD) investigation was carried out in a Rigaku SmartLab diffractometer equipped with a graphite monochromator. XRD pattern scanned in the range of 25-85 20 with a scan speed of 1° /min and step size of 0.01° . The average grain size was calculated by Scherrer's equation after eliminating the contribution of instrumental broadening of which determined using LaB₆ standard.

Vickers hardness of the alloys was obtained using a Mutitoyo hardness tester with a $100\,$ g applied load and $10\,$ s of dwelling time. The hardness tests were carried out at least $10\,$ times to calculate the average Vickers hardness.

2.3. Post corrosion surface characterization

X-ray photoelectron spectrometry (XPS) analysis was carried out to investigate the oxide film developed on the alloy surface. Samples were polished to 0.05 μm using colloidal silica and immersed in 0.1 M NaCl solution for 2 h. The oxide film investigation was conducted on 2 \times 2 mm scan area with a 60 take-off angle. Instrument chamber pressure was kept below 10^{-9} mbar and Mg anode was used as the X-Ray source of 300 W. CASA software was utilized to analyze XPS data and the background was eliminated using the Shirley function.

Time-of-flight secondary ion mass spectroscopy (ToF-SIMS) was performed to obtain elemental depth profiling on Al-5at%Fe 2 h immersed specimen in 0.1 M NaCl solution. The pressure of the main chamber inside the instrument was maintained below 10^{-9} mbar. Primary ion source of Bi $^{3+}$ with 25 keV and 0.35 pA target current was rastered over $100\times100~\mu m$ area. Cs $^+$ ion beam was used to sputter the surface with 1 keV and 7.2 nA current over $150\times150~\mu m$ area.

Surface was analyzed using SEM after 2 h, 24 h, and 7 days of immersion in 0.01 M NaCl. Both back scattered and secondary electron images were acquired and corroded regions were detected.

2.4. Electrochemical tests

Specimens were cold mounted into the epoxy resin and were ground with SiC emery paper to 400-600-800 grit under running water before the final grinding step of 1200 grit under ethanol. The interface between the metal and epoxy resin was sealed with a quick set epoxy resin to eliminate possible crevice corrosion. The samples were kept in a fume hood for 24 h prior to the electrochemical tests. Electrochemical tests were carried out in a conventional three-electrode flat-cell where a platinum mesh was used as a counter and a saturated calomel electrode (SCE) was used as the reference electrode. Electrochemical test was carried out using a Biologic VMP-300 multichannel potentiostat connected to a computer with EC-lab software. Electrochemical tests that performed in 0.01 M NaCl electrolyte (not deaerated). The open-circuit potential (OCP) was measured for 20 min after immersing the working electrodes to electrolyte. The CPP scans were obtained with a scan rate of 1 mV/s from 0.250 mV below the OCP. Reverse scans were performed until the anodic current density reached to 200 μA/cm². All the CPP tests were repeated at least three times to ensure reproducibility. Electrochemical impedance spectroscopy (EIS) for Al-5Fe alloy was performed in a 0.01 M NaCl solution with the application of a 10-mV amplitude AC sinusoidal voltage signal in the 100 kHz to 1 mHz frequency range after F. Ozdemir et al.

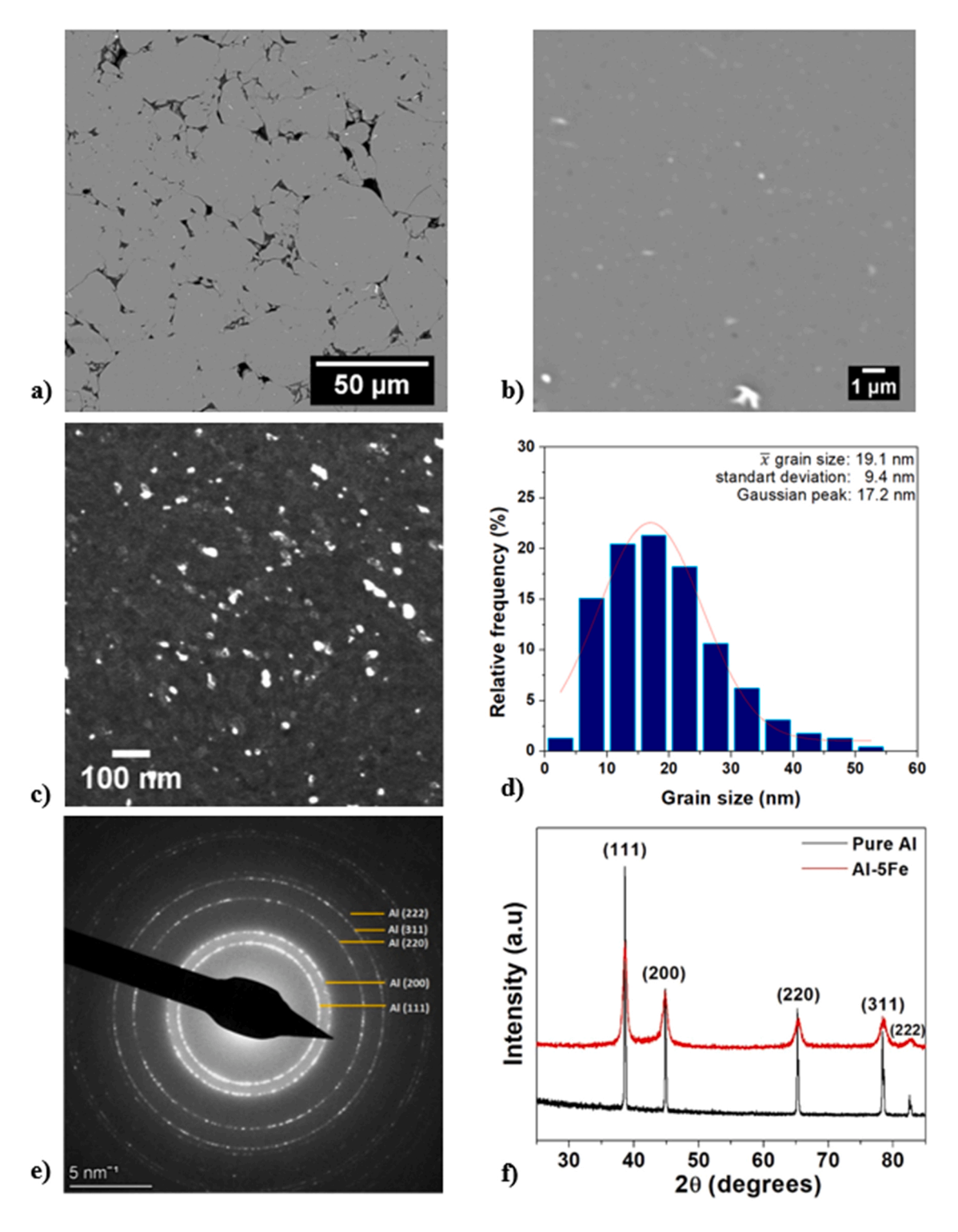


Fig. 1. Microstructural characterization of Al-5Fe alloy. a) BSE image of cold compacted Al-5Fe alloy b) High-magnification BSE image of Al-5Fe Alloy c) STEM-DF micrograph of Al-5Fe alloy d) Grain size distribution, estimated from the image presented in Appendix A, supplementary file e) SAED pattern of the Al-5Fe alloy f) XRD pattern of Al-5Fe alloy and Pure Al for the comparison.

12 h and 24 h exposure to electrolyte.

3. Results and discussion

3.1. Microstructure analysis

Backscattered electron (BSE) images of the high-energy ball milled

and subsequently consolidated Al-5Fe alloy are shown in Fig. 1.a. Consolidation was possible because of plastic deformation at the interparticle boundaries resulting in mechanical bonding. However, porosities were visible due to highly hardened particles with irregular shape. The high magnification SEM image (Fig. 1.b) shows a homogeneous microstructure free of coarse intermetallics. The BSE images and EDS analysis demonstrated the uniform dispersion of iron within the

F. Ozdemir et al. Corrosion Science 209 (2022) 110727

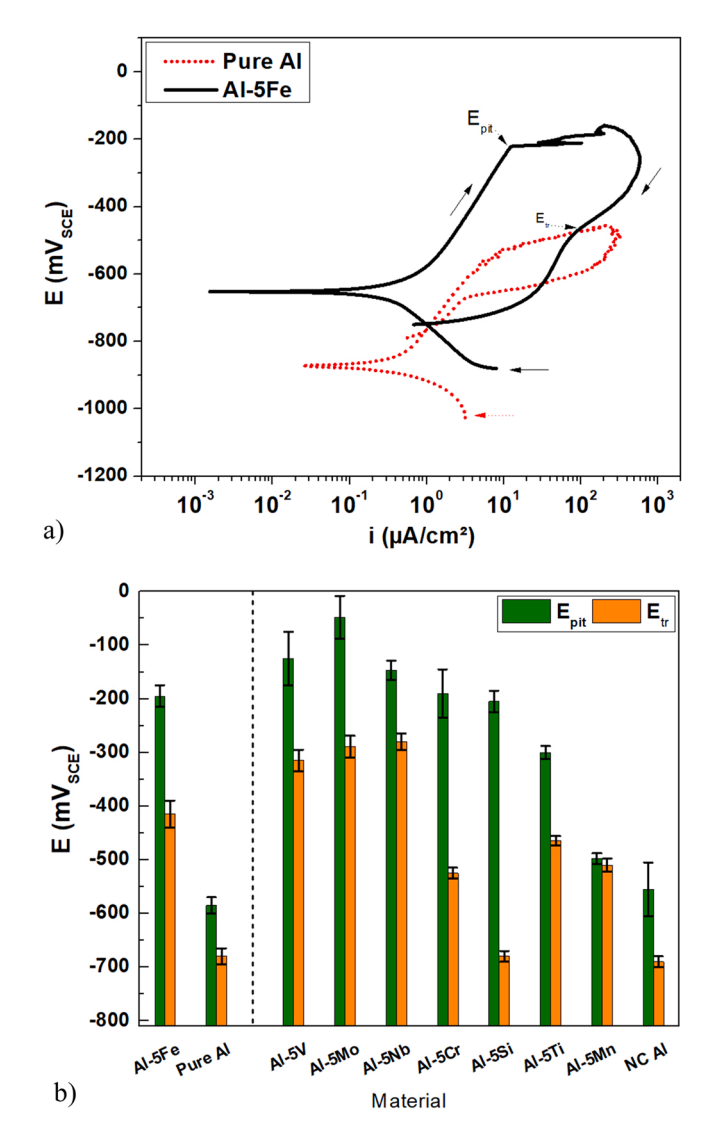


Fig. 2. Electrochemical characterization of Al-5Fe alloy. a) Representative CPP curves of Al-5Fe alloy and pure Al for the comparison in a 0.01 M NaCl electrolyte b) E_{pit} and E_{tr} for Al-5Fe alloy in comparison with E_{pit} and E_{tr} for HEBM Al-5 M (M: V, Mo, Nb, Cr, Si, Ti, Mn with 5 at%) and nanocrystalline aluminum (NC Al) [26].

aluminum matrix along with refined bright iron-rich particles. The STEM Dark field (DF) image of the Al-5Fe alloy is shown in Fig. 1.c, which shows presence of nano-sized grains in the microstructure. Dark field images were used estimate the grain size as shown in the Fig. 1d. The distribution of the grain size indicated a right skew and a mean grain size of 19.1 nm, indicating that the vast majority of the grains are below 20 nm. The selected area diffraction (SAED) pattern (Fig. 1.e) confirmed the alloy to be to be FCC Al (PDF Card -00 to 004-0787_Al) [39]. The lattice parameter through the (111) plane in the SAED pattern was calculated 4.0369 Å, while the lattice parameter for pure Al is 4.0495 Å. The decrease of the lattice parameter indicates the existence of smaller iron atoms in the substitutional lattice sites of aluminum. It can therefore be attributed to the formation of a supersaturated solid solution of iron in aluminum as a result of HEBM [40].

The X-ray diffraction patterns of the Al-5Fe alloy and pure Al are shown in Fig. 1.f. The XRD pattern shows all the characteristic peaks of Al in both samples, and the Fe-containing phases are not detected in the scan. This can be attributed to the combined effects of the increased solid solubility and the phases falling below the detection limit of the XRD. The XRD pattern shows a shift of the peaks towards higher 2θ

values compared to pure Al. For example, the (111) peak of the Al-5Fe alloy is shifted to 38.58° from 38.47°, and the lattice parameter of the Al-5Fe alloy decreased from 4.0495 Å to 4.0377 Å. This shift was attributed to the increased solubility of iron and the formation of an Al-Fe solid solution. The estimated solid solubility of iron in aluminum is calculated with reference to the published literature [5], which gave an estimated solid solubility of iron in aluminum to be ~2.53 at%, while using the data from the TEM investigation gave an estimated solubility of ~2.61 at%. The data from the XRD and TEM studies agree well and indicate the supersaturated solid solution of aluminum and iron. This increase in the solid solubility can be attributed to intense plastic deformation that resulted from the ball milling, causing defects such as grain boundaries and increased dislocation densities [41]. The defects when combined with local stresses, pave the way for the incorporation of iron into the structure and consequently substitution by Al atoms [40, 41]. Significant peak broadening was observed in the Al-5Fe alloy, which can be attributed to grain refinement and lattice strain due to the ball milling. The peak broadening was used to calculate the average grain size, which was 18.1 nm, similar to the value estimated using TEM. In close agreement, the XRD and TEM studies revealed a nanocrystalline structure and significantly increased iron solubility, which has a maximum solubility of 0.025 at% at 655 °C and negligible solubility at room temperature [42].

3.2. Corrosion behavior

Representative cyclic potentiodynamic polarization curves (CPP) of the Al-5Fe alloy along with pure Al are shown in Fig. 2.a. The experimental parameters and conditions were selected with reference to the work of Esquivel et al. [27] for the comparison of Al-5Fe alloy with Al-5 M (M: V, Mo, Nb, Cr, Si, Ti, Mn) alloys that were produced and characterized under the same conditions. The CPP curves show the effects of the iron addition on the corrosion behavior. A significant passive region was observed in the polarization curves of the Al-5Fe alloy. The pitting potential (Epit) at the breakdown of the passive film of the Al-5Fe alloy was significantly nobler (390 mV higher) than that of pure Al. The transition potential (E_{tr}) of the Al-5Fe alloy was 295 mV higher than the E_{tr} of pure Al. The E_{pit} and E_{tr} values for the tested alloys and for the Al-5 M alloys are presented in Fig. 2.b. The pure Al and nanocrystalline Al (NC Al) are also included in Fig. 2.b. The nobler pitting potential means more resistance against pitting corrosion. Etr indicates the ability of the alloys to repassivate after passive film breakdown. The influence of high-energy ball milling is clearly revealed in the comparison of NC Al with pure Al. The Al-5Fe alloy showed an increase in corrosion resistance, where E_{pit} and E_{tr} of Al-5Fe were nobler than Al-5Mn, Al-5Ti, Al-5Si, and Al-5Cr. Considering Epit, the corrosion resistance of the Al-5Fe alloy ranked after Al-5 V, Al-5Mo, and Al-5 Nb alloys.

Corrosion behavior of Al-5Fe alloy was investigated after immersion 0.01 M NaCl solution for 12 h and 22 h. Open circuit potential was measured during the immersion. The Bode and Nyquist plots of the Al-5Fe alloy after OCP stabilization of 12 and 24 h are shown in Fig. 3.a and 3.bb, respectively. The Al-5Fe alloy demonstrated time constants at high, medium and low frequencies that correspond to passive films at high and medium frequency and to localized corrosion at low frequency. The data was fitted using Zview software by employing the equivalent circuit model presented in Fig. 3.c. The obtained parameters for R_s (solution resistance), R_{film1}(film resistance 1), C_{film1} (capacitance of the film 1), R_{film2} (film resistance of film 2), R_{ct} (charge transfer resistance) and CPE values (constant phase elements) which represent deviation from ideal capacitance are presented in Table 1. The model suggests two layered passive films. The resistance of the film at outer layer was 59 Ω . cm² and 58 Ω .cm² after 12 h and 24 h of exposure, respectively. The resistance of the film closer to metal was 5.7 k Ω .cm² after 12 h and increased to $7 \text{ k}\Omega.\text{cm}^2$ after 24 h of exposure which is an indicator of increased corrosion resistance with the increased exposure time. In addition, the Rct value which indicates the resistance to localized

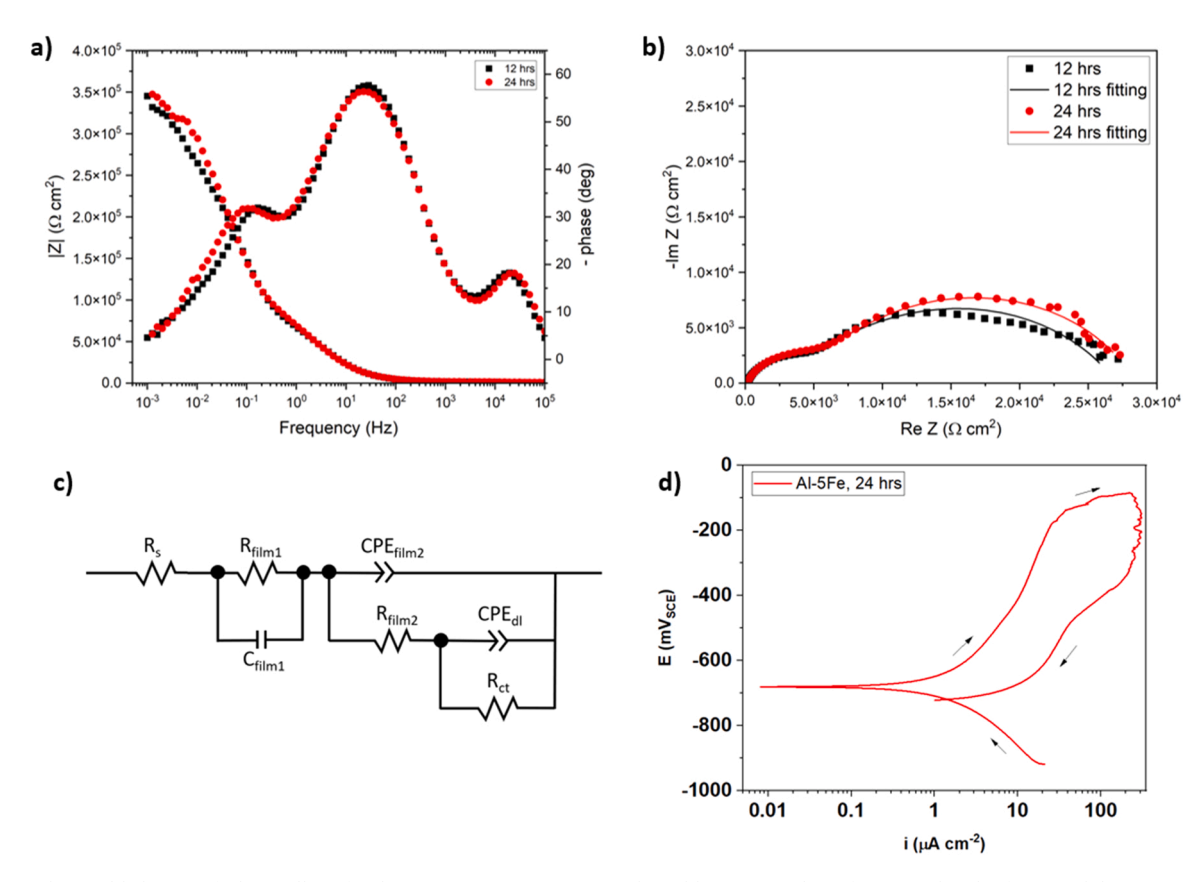
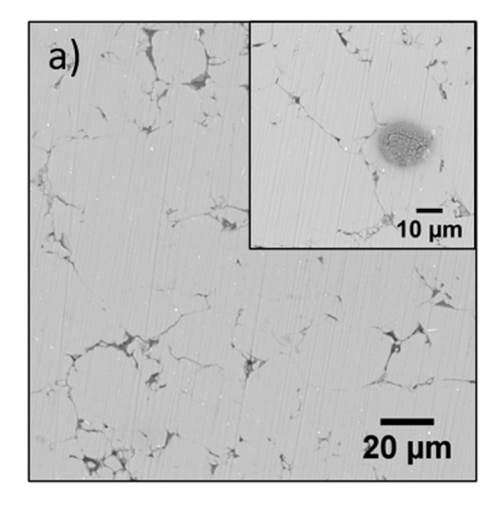


Fig. 3. Electrochemical behavior of Al-5Fe alloy after longer immersion time. a) Bode and b) Nyquist plots after 12 and 24 h of OCP stabilization in 0.01 M NaCl solution. c) The equivalent circuit model used for EIS data fitting for Al-5Fe alloy and d) Representative CPP curve after 24 h of immersion in 0.01 M NaCl.

Table 1
Representative values of the equivalent electrical circuit of fitting of impedance spectra of Al-5Fe alloys after 12 and 24 h of immersion in 0.01 M NaCl.

	Rs (Ω.cm ²)	R_{film1} (Ω cm ²)	C _{film1} (μF cm ⁻²)	CPE _{film2} (μF cm ⁻²)	CPE _{film2-p}	R_{film2} (k Ω cm ²)	CPE _{dl} (μF cm ⁻²)	CPE _{dl-p}	R_{ct} (k Ω cm ²)	${\it Chi-Squared}(x10^{-2})$
12 h	76	59	0.2	17.0	0.8	5.7	135.1	0.7	21.2	0.07
24 h	76	58	0.1	20.6	0.8	7.0	160.4	0.7	21.3	0.02



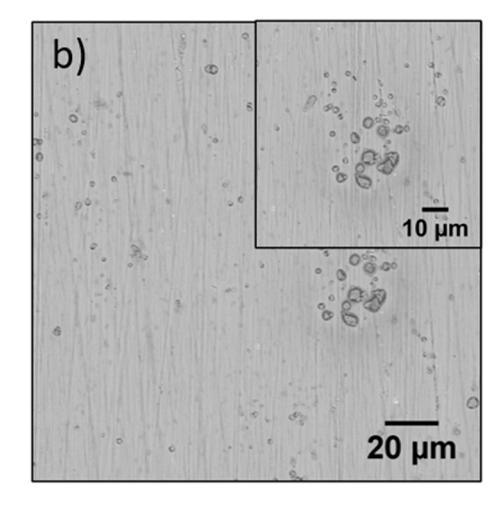


Fig. 4. BSE images of a) Al-5Fe alloy and b) Pure Al, after immersion in 0.01 M NaCl for 24 h.

corrosion was not decreased after 24 h and indicated a slight increment (from 21.2 to 21.3 k Ω .cm²). The corrosion performance after prolonged immersion was further investigated with cyclic potentiodynamic

polarization after 24 h of immersion and presented in Fig. 3.d. The polarization results show E_{pit} (around $-120\ mV)$ which is higher than the one presented at Fig. 2 and Pure Al (Epit $\sim\!-400\ mV)$ tested in same

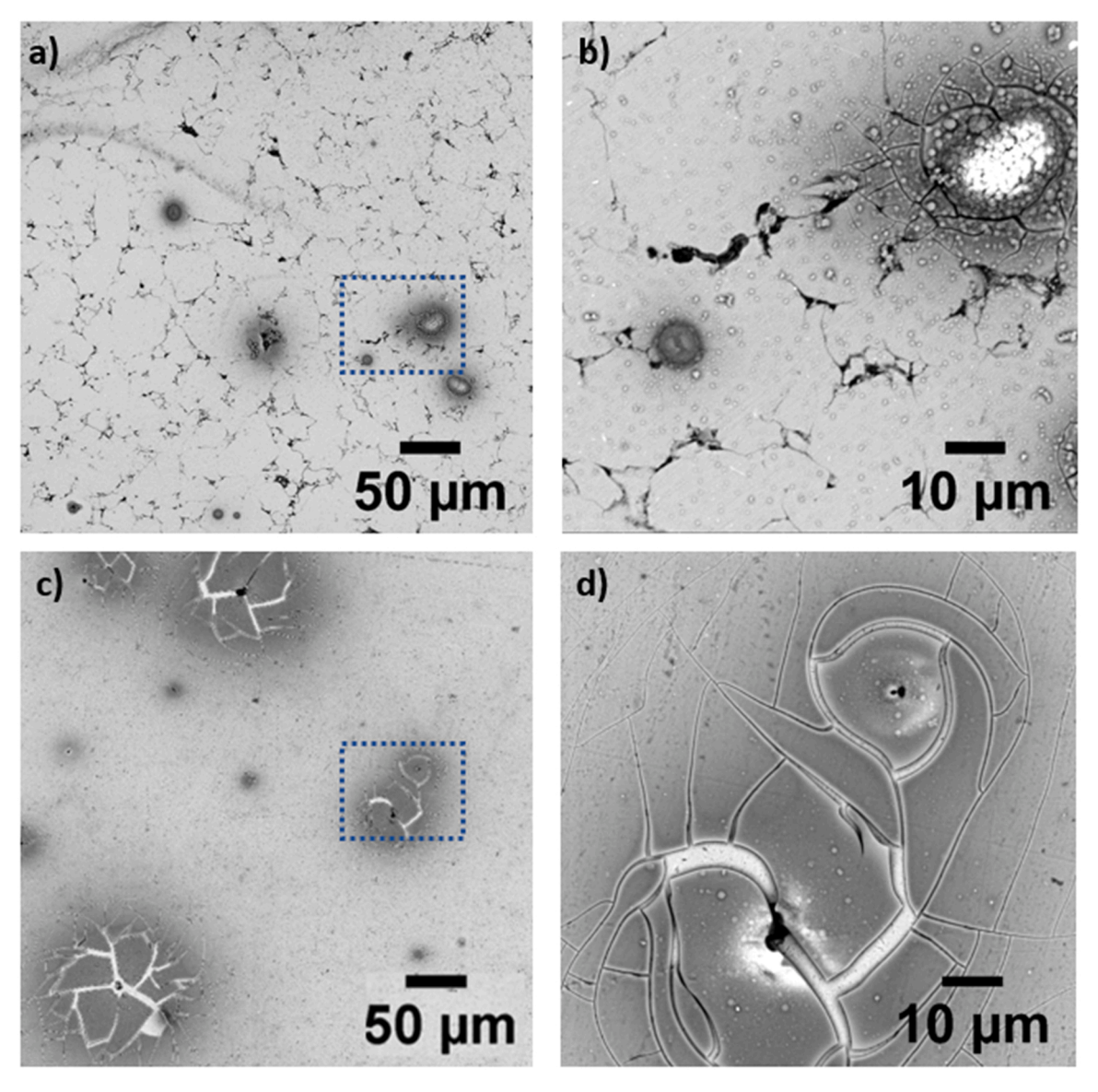


Fig. 5. BSE images of a) and b) Al-5Fe alloy, c) and d) Pure Al, after immersion in 0.01 M NaCl for 7 days.

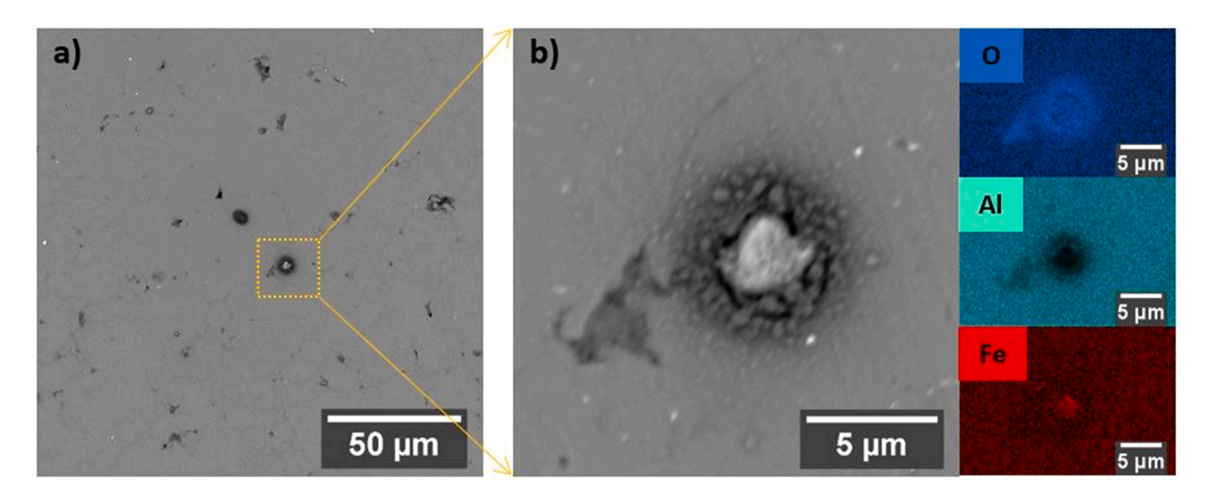
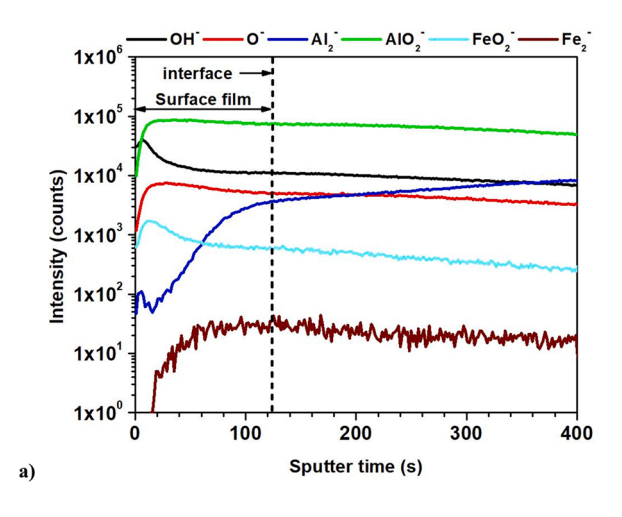


Fig. 6. a) SEM-EDS micrographs (BSE) of the Al-5Fe alloy immersed in 0.1 M NaCl solution for 2 h b) Higher magnification image of the region shown by yellow box with EDS mapping.



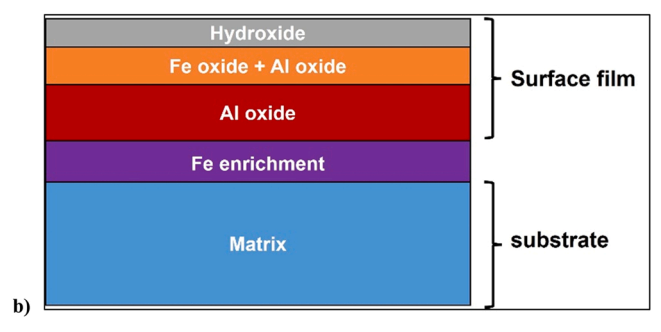


Fig. 7. Surface film investigation of the Al-5Fe alloy after the immersion in $0.1\,\mathrm{M}$ NaCl solution for $2\,\mathrm{h}$. a) ToF-SIMS data showing the negative ion depth profiles with respect to sputter time. b) Schematic representation of layered model of the surface film.

conditions (Supplementary, S2).

The BSE images of Al-5Fe alloy along with Pure Al after immersion in 0.01 M NaCl electrolyte for 24 h are presented in Fig. 4.a and b, respectively. The Al-5Fe alloy, despite having surface porosity, showed less pitting compared to Pure Al. The BSE images of the Al-5Fe alloy and Pure Al immersed in 0.01 M NaCl electrolyte for 7 days are presented in Fig. 5. Al-5Fe alloy showed better corrosion response in terms of size and number of pits per unit are after prolonged exposure to the NaCl electrolyte. The higher magnification images of Al-5Fe and Pure Al (Fig. 6.b and 6.d) shows corrosion products and cracks on the surface. The size and number of cracks were less in the Al-5Fe alloy compared to Pure Al that indicates better corrosion resistance of Al-5Fe alloy even after 7 days of immersion. The size, and morphology of the pits are in accordance with the high-energy ball milled alloys, which can be attributed to a absence of course intermetallics [27,29]. SEM analysis after immersion tests (Figs. 4 and 5) corroborated the electrochemical data (Figs. 2 and 3) showing high corrosion resistance in Al-5Fe alloy. Surface of Al-Fe alloy was further examination by SEM and EDS after 2 h immersion to understand the corrosion initiation (Fig. 4). The zoomed image with EDS mapping (Fig. 4.b) shows that the pits formed in the form of trenches and initiated around the Fe-rich particle, which is cathodic to the matrix. The lack of coarse Fe intermetallics and constitutional particles resulted in high corrosion resistance as confirmed by electrochemical tests.

3.3. Surface film characterization

The surface film investigation of the Al-5Fe alloy by ToF-SIMS is presented in Fig. 7. The negative ion intensities versus sputter time for the Al-5Fe alloy is plotted in Fig. 7.a. The SIMS analysis for the Al-5Fe alloy shows the depth profiles for OH, $^{18}O^{-}$, Al $_{2}$, AlO $_{2}$, FeO $_{2}$, where Al $_{2}$ and Fe $_{2}$ ions represent Al and Fe in metallic state, respectively, while

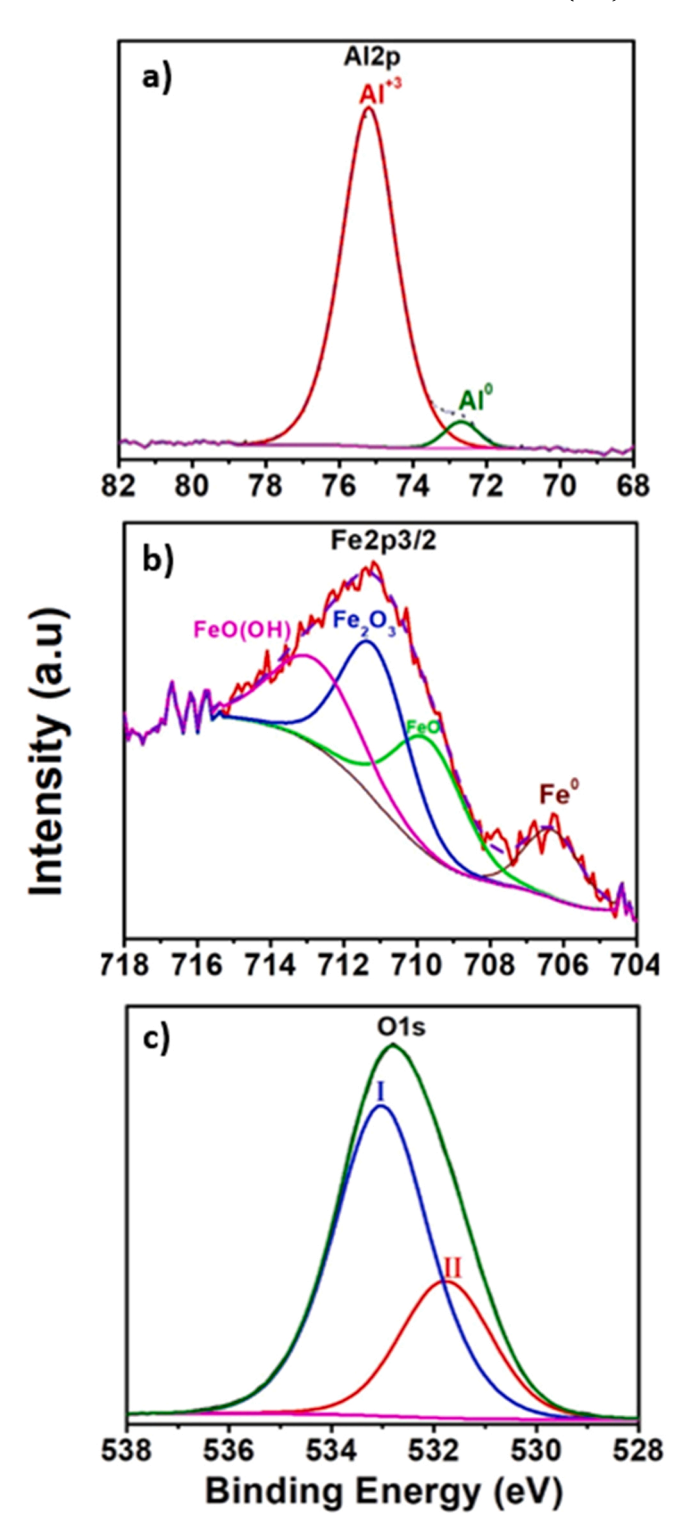


Fig. 8. XPS high-resolution regional scan of a) Al2p, b) Fe2p3/2 and c) O1s peaks showing the metallic and oxidized species.

 AlO_2 and FeO_2 ions correspond to Al and Fe in oxidized state, respectively. The $^{18}O^-$ is selected as the representative for oxygen due to the saturation of the detector in the case of $^{16}O^-$ selection [43]. The depth profile can be divided into two main zones: Surface film and alloy substrate, which is divided with a dashed line indicated as the interface. In the initial phase of sputtering, a rapid increase in metallic ion intensity is observed, which tends to stabilize with increasing sputtering time. The alloy substrate begins when the Al^- ion reaches a plateau and remains constant. The surface film can be identified up to about 120 s

Table 2Binding energies (BE), full-widths at half maximum (FWHM) and intensities (in atomic percent) of the Al-5Fe alloy after 2 h immersion in 0.1 M NaCl.

Peak	BE (eV)	FWHM	Intensity (at%)
O(I)	533.03	2.2	51.16
O(II)	531.77	2.1	21.47
Al^{3+}	75.20	1.7	24.89
Al^0	72.69	1.1	1.21
FeO	709.68	2.3	0.35
Fe_2O_3	711.16	2.2	0.44
FeO(OH)	712.79	2.8	0.32
Fe ⁰	706.31	1.8	0.16

sputter time. The Fe⁻ ion appears to show a slight hump at the interface, which is attributed to Fe enrichment at the metal/film interface. This phenomenon is also reported in other literature where the solute enrichment is observed due to the rapid oxidation kinetics of Al [33,44]. A simplified layered model is illustrated in Fig. 7.b to understand the elemental distribution. The surface film consists mainly of Al oxide with Fe oxide located at the top portion, while the metallic Fe enrichment is located at the metal/film interface.

The passive film was further investigated using XPS after the immersion in 0.1 M NaCl for 2 h. Al, O, and Fe peaks were detected in the XPS survey scan of the Al-5Fe alloy. The high-resolution regional scans of the Al2p, Fe2p3/2 and O1s peaks of the Al-5Fe alloy are shown in Fig. 8. The binding energies (BE), full width half maximum (FWHM), and intensities (in atomic percent) of the species are reported in Table 2. The Al2p peak (in Fig. 8.a) showed peaks at two binding energies, metallic Al (Al⁰) with a lower binding energy at 72.69 eV and Al oxide/ hydroxide (Al³⁺) with a higher binding energy at 75.2 eV. The O1s peak shown in Fig. 5.c was compromised of two peaks (I and II), where O(I) is attributed to hydroxide or carbon bonded with oxygen obtained at a higher binding energy of 533.03 eV and O(II) is coming from the oxide contribution obtained at a lower binding energy of 531.77 eV [32,45]. The high-resolution peak corresponding to Fe2p3/2 is presented in Fig. 8.b, which is deconvoluted into four peaks: FeO(OH) (712.79 eV), Fe_2O_3 (711.16 eV), FeO (709.68 eV), and metallic Fe^0 (706.1 eV). Fe_2O_3 had the highest intensity among the three oxides, followed by FeO(OH) and FeO. The elemental concentration of Al oxide thickness on the surface of Al-5Fe alloy was estimated by the XPS investigation, and the oxide thickness was 7 nm, calculated with the help of the method reported in the literature [46]. The estimation by XPS survey illustrates

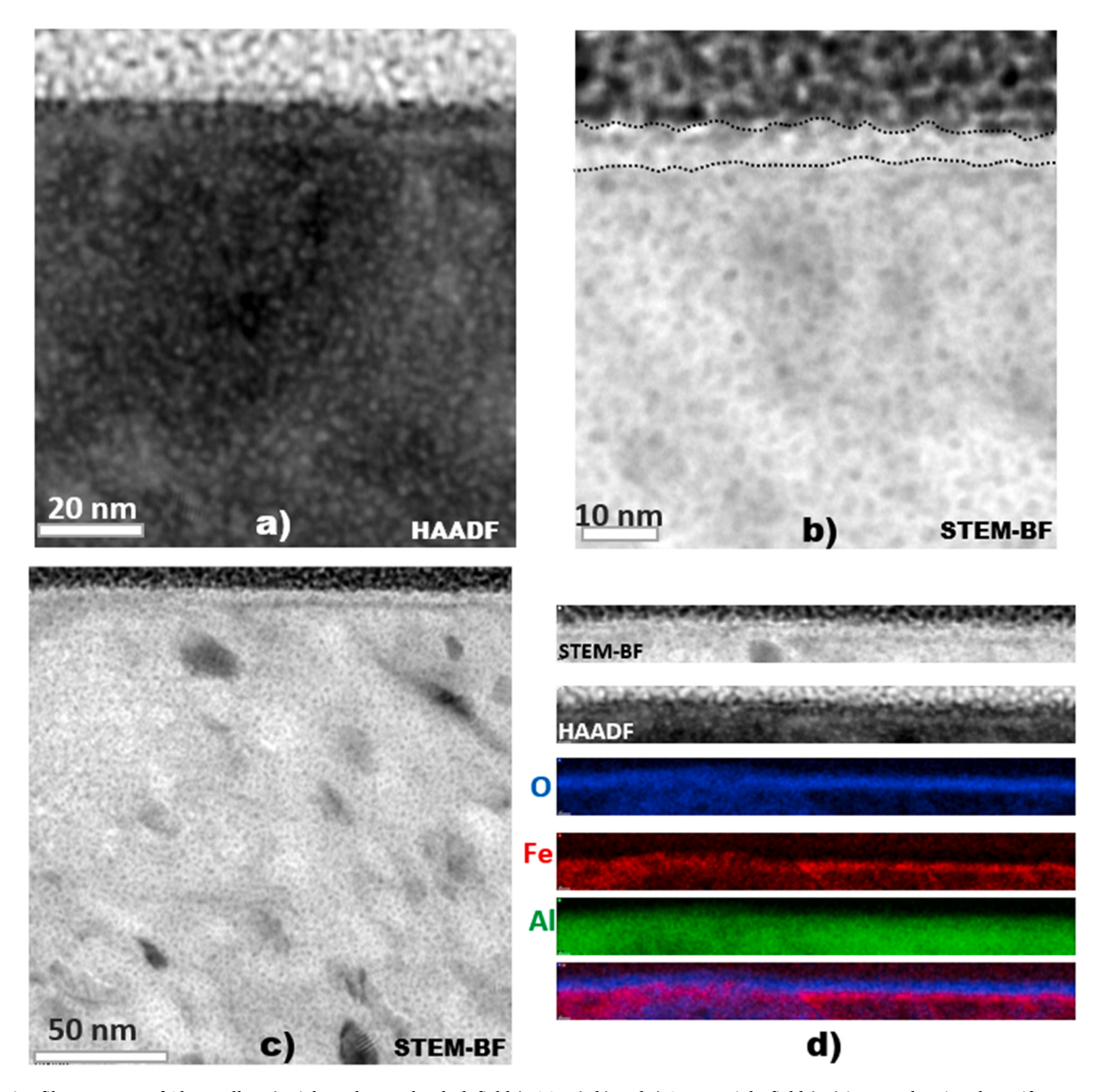


Fig. 9. Passive film structure of Al-5Fe alloy a) High angle annular dark field (HAADF), b) and c) STEM Bright field (BF) images showing the uniform passive film, d) STEM-BF and HAADF images and EDS elemental mapping for Al, Fe, O; taken from c).

Table 3Elemental concentration (%at.) and the Al oxide thickness on the surface of Al-5Fe alloy estimated by XPS survey for 2 h immersion in 0.1 M NaCl.

	O 1 s	Al 2p	Fe2p	O/Al	Al Oxide thickness
Al-5Fe	71.83	27.33	0.84	2.62	7.03 nm

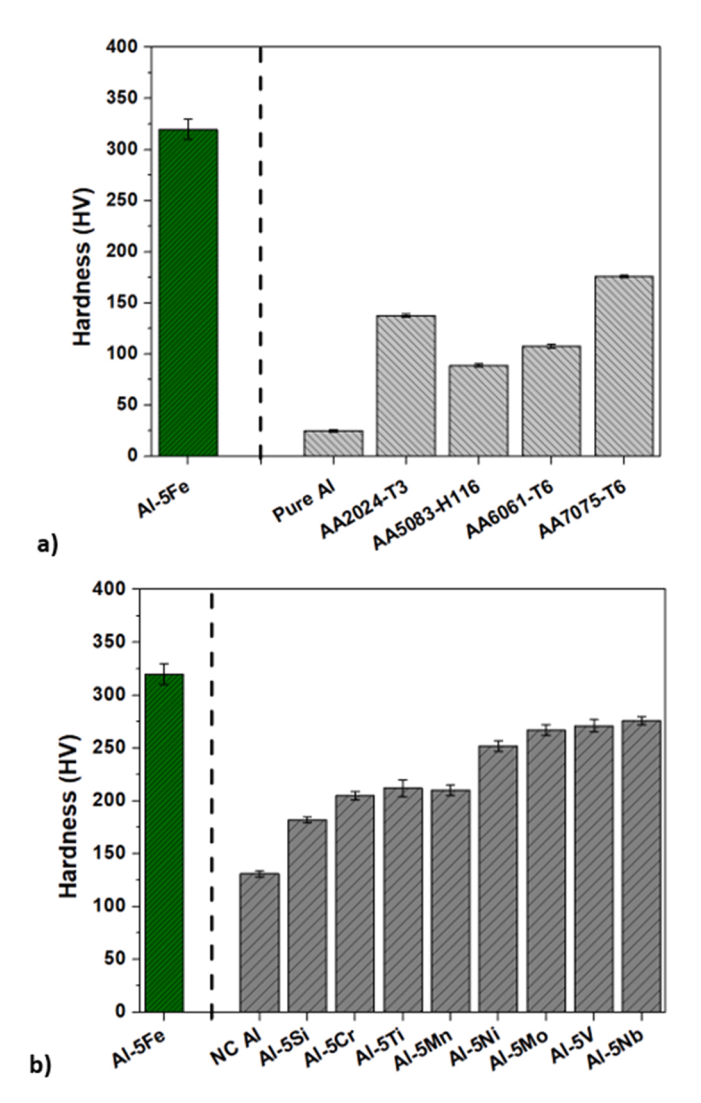


Fig. 10. Plot of Vickers hardness a) Comparison of Al-5Fe with pure Al, AA2024-T3, AA5083-H116, AA6016-T6, AA7075-T6 b) Comparison of Al-5Fe with nanocrystalline Al (NC Al) and Al-5 M alloys (M: Si, Cr, Ti, Mn, Ni, Mo, V, Nb with 5 at%).

that the oxide film was a combination of O, Al, and Fe. The oxide to Al ratio was estimated to be 2.62, which is about 1.75 times higher than the stoichiometric value of Al_2O_3 . The higher stoichiometric ratio can be attributed to the additional presence of iron oxides along with the hydroxides. Moreover, the theoretical ratio of as-added metallic Fe/Al (5/95 at%) should be 0.05 but the surface shows the ratio to be 0.13 which signifies the strong contribution coming from the Fe enrichment at the metal/film interface.

STEM cross-sectional images of the passive film for the Al-5Fe alloy after 2 h of immersion in 0.1 M NaCl solution are shown in Fig. 9. In Fig. 9.b, the passive film is shown and indicated by dotted lines. The average thickness of the passive film was around 7 nm and agreed with the estimated data from XPS analysis (Table 3). The EDS mapping obtained from the zone in Fig. 9.c indicated the distribution of O on top of the alloy (Fig. 9.d) and therefore verified the uniformly formed passive

film. Additionally, the Fe enrichment is observed at the metal/film interface that is in correlation with TOF-SIMS and XPS investigation.

3.4. Hardness

The hardness of the Al-5Fe alloy is presented in Fig. 10. The Al-5Fe alloy with an average hardness of 319 HV, showed significantly higher hardness compared to commercially available high-strength aluminum alloys, as shown in Fig. 10.a. The hardness of the Al-5Fe alloy was also compared with nanocrystalline Al-5 M alloys that were prepared by high-energy ball milling (Fig. 10.b) [27], where the Al-5Fe alloy showed a superior value than reported Al-5 M alloys, which can be attributed to the combined influences of grain refinement, enhanced solute solution and uniform dispersion of secondary phases.

4. Discussion

The Al-5Fe alloy investigated in this study exhibited superior hardness and corrosion resistance. Compared to pure Al, the corrosion resistance of the Al-5Fe alloy was significantly higher due to the synergistic effect of extended solid solubility and a nanocrystalline structure known for its advantage on the passivation capabilities of the alloys [47–49]. This study is new and interesting from both technological and scientific perspectives. The alloying elements reported to improve corrosion performance in nonequilibrium Al alloys are based on expensive elements such as Cr, Ni, Ti, V, Mn, Nb, and Ta which lead to high material costs. Considering the elemental costs of the alloys calculated based on the data presented in [50]; the cost of the Al-5Fe alloy (~1.75 \$/kg), is significantly lower than other binary alloys such as Al-5 V (~3.78 \$/kg), Al-5 Nb (~8.06 \$/kg) and Al-5Mo (~4.13 \$/kg).

Fe is known for its deleterious effects on the corrosion performance of the Al alloys, and its content accumulates continuously during primary and secondary processing of aluminum. Therefore, it requires close control to monitor the Fe content, which is highly challenging to refine from the alloy. Considering the material cost of Fe and the efforts made to refine from the microstructure, the Al-5Fe alloy results were very promising for the direct employment of high Fe-containing materials as high-performance alloys. In addition, it should be cognizant of the fact that recycling, which is critical for sustainability, introduces Fe [51] and therefore reduces the corrosion performance of the alloys and limits the use of recycled Al in several applications [7,52,53]. The results of this study indicate that a bulk Al alloy with high Fe content and high corrosion resistance can be produced, which is promising for recycling of Al alloys.

The intermetallic compounds of Al-Fe in the ball milled alloy were refined and therefore the unfavorable effects were eradicated [54]. The extended solid solution of Fe in Al appears to cause significant improvement in corrosion performance. Additionally, the electrochemical potential difference between cathodic Fe-intermetallic compounds and the Fe-rich matrix could be decreased, which resulted in decreased galvanic activity and therefore higher pitting corrosion resistance [55].

The high corrosion resistance of the ball milled alloys is attributed to one or more of the following mechanisms proposed in the literature [27, 32]: Improved passivity by enrichment of alloying element at metal/film interface, improved ability of alloy for repassivation, release of corrosion inhibiting compounds., and higher vacancy annihilation due to solute ion doped passive layers. The modification in the passive film of Al-5Fe alloy was demonstrated by XPS and SIMS studies. The surface film showed the presence of metallic and oxidized Fe in the passive film of Al-5Fe alloy. The presence of Fe in oxidized state within the passive film could lead to a change in the number of oxygen vacancies, which can be attributed to the formation of low mobility species [32]. In addition, SIMS and XPS studies did not reveal the presence of chloride in the passive film structure. The Cl incorporation is known to be a token

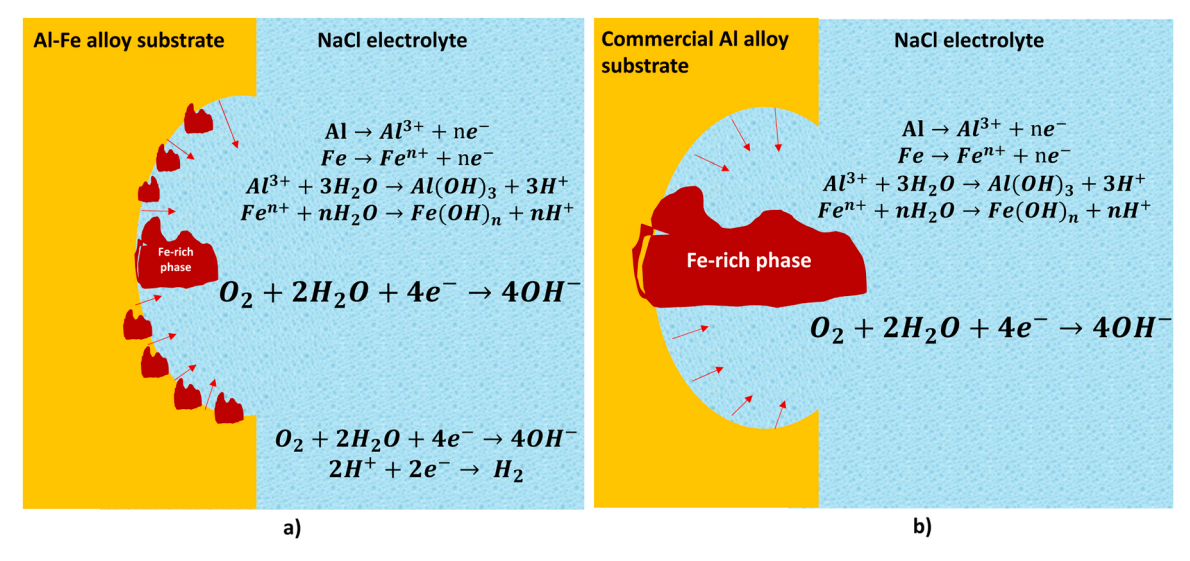


Fig. 11. Schematic representations of the effect of microstructure on pit growth and repassivation: a) localized corrosion in ball milled Al-5Fe alloy, b) localized corrosion in conventional Al alloys. Arrow shows the oxidation of Al and Fe. The hydrolysis of ions causes decrease in pH. Cathodic reaction occurs at particles shown in red color.

for the localized Al corrosion [56-58] and the absence of chloride could be attributed to the Fe in the passive film that interferes with the Cl incorporation, which needs further focused research. Witharamage et al. [32] and Christudasjustus et al. [33] attributed the improved corrosion resistance to either an additional barrier from metallic V enrichment or deposition of V in the form of vanadate on cathodic phases in the nanocrystalline Al-V alloy. The solute enrichment at the metal/film interface in Al-Fe alloy (Fig. 8.d) is similar to the aforementioned works however suggests different mechanisms. In all likelihood, Fe enrichment at the metal/passive film interface causes an extra Fe oxide layer that provides an obstacle to formation of the pit. Therefore, it is more likely to suggest two mechanisms in Al-5Fe alloy in improving the corrosion resistance: 1) presence of Fe enrichment at metal/film interface that hinder the penetration of chloride ions, and 2) decrease in potential difference between cathodic particle and the matrix due to enhanced solid solution. In alloys containing alloying elements such V, Mo etc. can be considered to release corrosion inhibiting species such as vanadates and molybdates. However, this hypothesis may not be applicable to Al-Fe alloys.

An additional corrosion mechanism causing repassivation at early stages of corrosion could be proposed based on the unique microstructure and distribution of cathodic sites in the matrix of ball milled Al-5Fe alloy. The uniformly distributed Fe-rich phases would be exposed within the pits and they would act as cathodic sites (Fig. 11.a). Cathodic reaction would either be water reduction, oxygen reduction or H+ reduction depending on the local pH and potential. Either of these cathodic reactions would suppresses acidification below a critical level and prevent formation of critical pit solution (CPS)- necessary for pit growth. Absence of CPS would cause the repassivation in early stages of corrosion which will result in higher pitting potential and higher repassivation. This condition encountered in ball milled Al-5Fe alloy is different than conventional pits in commercial Al alloys, where cathoodic and anodic sites are separated (Fig. 11.b). Cathodic sites can be imagined to be present outside the pit which produces hydroxyl ions near the passive surface and destabilize it to form trench. During pit growth, the cathodic reaction could be considered to be centered on cathodic particles and dissolution of pits occurs. This hypothesis of increasing corrosion resistance by introducing fine cathodic sites within pits needs to be tested experimental. If this is a valid hypothesis then it could be used to design new corrosion resistant alloys and explain pitting and repassivation mechanisms in alloys with far-from-equilibrium microstructures and compositions.

The Al-5Fe alloy investigated herein showed the highest hardness among Al-5 M alloys, along with significant corrosion performance, ranking after V, Mo, and Nb. This high strength can be attributed to the uniform dispersion of refined Al-Fe intermetallics, significant grain refinement, and the enhanced solid-state solubility of iron [59–62]. The strengthening mechanisms that contribute to the overall strength of the Al-5Fe alloy can be estimated by quantifying the individual contribution of each mechanism are presented in Table 4 and discussed in the supplementary document. The primary contribution is due to grain boundary strengthening (σ_{gb}) followed by solid solution strengthening (σ_{ss}). The other contributions to overall strength (σ_{Other}) includes strength contribution due to fine precipitates by Orowan strengthening σ_{Orowan} and contributions from dislocations [8,29,63,64].

5. Conclusions

Nanocrystalline Al-5Fe alloy was successfully produced by highenergy ball milling followed by consolidation through roomtemperature compaction. The Al-5Fe alloy exhibited extended solid solubility of Fe in Al and homogeneous microstructure free from coarse intermetallics. The alloy exhibited high strength due to the enhanced solid solubility of Fe, ultra-fine grain refinement, and uniform distribution of Al-Fe intermetallics.

The Al-Fe alloys showed high pitting corrosion resistance as investigated using cyclic potentiodynamic polarization test. Surface characterization using STEM, XPS and SIMS revealed formation of Al-rich passive film with Fe enrichment at the surface film/substrate interface. The improvement in the corrosion performance of Al-5Fe alloy was

Table 4Estimated different strengthening contributions to the yield strength of Al-5Fe alloy.

	σ_{gb} (MPa)	σ_{ss} (MPa)	σ_{other} (MPa)	$\sigma_y(estimated)$ (MPa)	$\sigma_y(experimental)$ (MPa)
Al-5Fe	709	230	225	1160	1078

attributed to the following factors:

- Combined influences of the microstructure with high solid solubility of Fe and absence of coarse intermetallics.
- The decrease in the galvanic activity between matrix and cathodic particles, and additional barrier due to the Fe enrichment at the metal/film interface.
- The modification in the passive film structure due to the incorporation of Fe and thus the improved ability to re-passivate.
- Presence of uniformly distributed fine cathodic sites within the pits and therefore suppression of the critical pit solution formation.
 Cathodic particles within the pits are hypothesized to consume H⁺ ions or produce OH⁻ ions which do not allow the pH to drop below a critical limit needed for the pit growth.

CRediT authorship contribution statement

F. Ozdemir: Conceptualization, Methodology, Investigation, Formal analysis, Data curation, Writing - original draft, Writing - review & editing. CS. Witharamage: Investigation, Formal Analysis, Writing - review & editing J. Christudasjustus: Methodology, Investigation, Formal analysis, Writing - review & editing. Ahmed A. Darwish: Investigation, Formal analysis, Writing - review & editing. H. Okuyucu: Resources. R.K. Gupta: Conceptualization, Methodology, Writing - original draft, Writing - review & editing, Supervision, Project administration, Resources, Funding acquisition.

Declaration of Competing Interest

The authors declare that they have no known competing financial interests or personal relationships that could have appeared to influence the work reported in this paper.

Data availability

All data included in this study are available upon reasonable request by contacting the corresponding author.

Acknowledgements

The financial support from the National Science Foundation (NSF-CMMI 1760204 and NSF-CMMI 2131440) under the direction of Dr. Alexis Lewis is highly acknowledged. Furkan Ozdemir acknowledges the support by the Scientific and Technological Research Council of Türkiye (TUBITAK). The authors acknowledge the Analytical Instrument Facility (AIF) at North Carolina State University supported by the State of North Carolina and the National Science Foundation (award number ECCS-2025064).

Appendix A. Supporting information

Supplementary data associated with this article can be found in the online version at doi:10.1016/j.corsci.2022.110727.

References

- [1] J.R. Davis, Corrosion of aluminum and aluminum alloys, in: ASM Int., 2000: pp. 1–24. https://doi.org/10.1361/caaa1999p001.
- [2] I.J. Polmear, Light Alloys, Butterworth-Heinemann, 2005, https://doi.org/ 10.1016/B978-0-7506-6371-7.X5000-2.
- [3] T.S. Srivatsan, A review of: "DISPERSION STRENGTHENED ALUMINUM ALLOYS" edited by Y.-W. Kim and W.M. Griffith TMS, Warrendale, Pennsylvania 795 pages, hardcover, 1988, Mater. Manuf. Process. 6 (1991) 565–568. https://doi.org/ 10.1080/10426919108934788.
- [4] K.E. Knipling, D.C. Dunand, D.N. Seidman, Criteria for developing castable, creepresistant aluminum-based alloys – a review, in: Int. J. Mater. Res, 97, 2006, pp. 246–265, https://doi.org/10.3139/ijmr-2006-0042.

- [5] D.K. Mukhopadhyay, C. Suryanarayana, F.H. (SAM. Froes, Structural evolution in mechanically alloyed Al-Fe powders, Metall. Mater. Trans. A 26 (1995) 1939–1946, https://doi.org/10.1007/BF02670665.
- [6] K. Nişancıoğlu, Electrochemical behavior of aluminum-base intermetallics containing iron, J. Electrochem. Soc. 137 (2019) 69–77, https://doi.org/10.1149/ 1.2086441.
- [7] T. Dorin, N. Stanford, N. Birbilis, R.K. Gupta, Influence of cooling rate on the microstructure and corrosion behavior of Al-Fe alloys, Corros. Sci. 100 (2015) 396–403, https://doi.org/10.1016/j.corsci.2015.08.017.
- [8] X. Qi, N. Takata, A. Suzuki, M. Kobashi, M. Kato, Change in microstructural characteristics of laser powder bed fused Al-Fe binary alloy at elevated temperature, J. Mater. Sci. Technol. 97 (2022) 38–53, https://doi.org/10.1016/j. ipst 2021.04.038
- [9] W. Wang, N. Takata, A. Suzuki, M. Kobashi, M. Kato, High-temperature strength sustained by nano-sized eutectic structure of Al–Fe alloy manufactured by laser powder bed fusion, Mater. Sci. Eng. A 838 (2022) 1–5, https://doi.org/10.1016/j. msea.2022.142782.
- [10] T.T. Sasaki, T. Ohkubo, K. Hono, Microstructure and mechanical properties of bulk nanocrystalline Al-Fe alloy processed by mechanical alloying and spark plasma sintering, Acta Mater. 57 (2009) 3529–3538, https://doi.org/10.1016/j. actamat.2009.04.012.
- [11] S.S. Nayak, M. Wollgarten, J. Banhart, S.K. Pabi, B.S. Murty, Nanocomposites and an extremely hard nanocrystalline intermetallic of Al-Fe alloys prepared by mechanical alloying, Mater. Sci. Eng. A. 527 (2010) 2370–2378, https://doi.org/ 10.1016/j.msea.2009.12.044
- [12] K. Ma, H. Wen, T. Hu, T.D. Topping, D. Isheim, D.N. Seidman, E.J. Lavernia, J. M. Schoenung, Mechanical behavior and strengthening mechanisms in ultrafine grain precipitation-strengthened aluminum alloy, Acta Mater. 62 (2014) 141–155, https://doi.org/10.1016/J.ACTAMAT.2013.09.042.
- [13] J.M. Cubero-Sesin, M. Arita, Z. Horita, High strength and electrical conductivity of Al-Fe alloys produced by synergistic combination of high-pressure torsion and aging, Adv. Eng. Mater. 17 (2015) 1792–1803, https://doi.org/10.1002/ adem.201500103.
- [14] O.N. Senkov, F.H. Froes, V.V. Stolyarov, R.Z. Valiev, J. Liu, Microstructure of aluminum-iron alloys subjected to severe plastic deformation, Scr. Mater. 38 (1998) 1511–1516, https://doi.org/10.1016/S1359-6462(98)00073-6.
- [15] R.K. Gupta, B.S. Murty, N. Birbilis, An Overview of High-energy Ball Milled Nanocrystalline Aluminum Alloys, Springer, 2017, https://doi.org/10.1007/978-3-319-57031-0.
- [16] T.T. Sasaki, T. Mukai, K. Hono, A high-strength bulk nanocrystalline Al-Fe alloy processed by mechanical alloying and spark plasma sintering, Scr. Mater. 57 (2007) 189–192, https://doi.org/10.1016/j.scriptamat.2007.04.010.
- [17] J.R. Davis, Aluminum and Aluminum Alloys, in: Alloy. Underst. Basics, ASM International, 2001, pp. 351–416, https://doi.org/10.1361/autb2001p351.
- [18] M.K. Cavanaugh, J. Electrochem, C. Soc, M.K. Cavanaugh, J. Li, N. Birbilis, R.G. Buchheit, Electrochemical Characterization of Intermetallic Phases Common to Aluminum Alloys as a Function of Solution Temperature Electrochemical Characterization of Intermetallic Phases Common to Aluminum Alloys as a Function of Solution Temperature, (2014). https://doi.org/10.1149/2.0361412jes
- [19] J. Li, N. Birbilis, R.G. Buchheit, Electrochemical assessment of interfacial characteristics of intermetallic phases present in aluminium alloy 2024-T3, Corros. Sci. 101 (2015) 155–164, https://doi.org/10.1016/j.corsci.2015.09.012.
- [20] A.E. Hughes, R. Parvizi, M. Forsyth, Microstructure and corrosion of AA2024, Corros. Rev. 33 (2015) 1–30, https://doi.org/10.1515/corrrev-2014-0039.
- [21] N. Birbilis, M.K. Cavanaugh, R.G. Buchheit, Electrochemical behavior and localized corrosion associated with Al7Cu2 Fe particles in aluminum alloy 7075-T651, 48 (2006) 4202–4215. https://doi.org/10.1016/j.corsci.2006.02.007.
- [22] L.C. Abodi, J.A. Derose, S. Van Damme, A. Demeter, T. Suter, J. Deconinck, Modeling localized aluminum alloy corrosion in chloride solutions under nonequilibrium conditions: Steps toward understanding pitting initiation, Electrochim. Acta 63 (2012) 169–178, https://doi.org/10.1016/j.electacta.2011.12.074.
- [23] J. Esquivel, R.K. Gupta, Review—corrosion-resistant metastable al alloys: an overview of corrosion mechanisms, J. Electrochem. Soc. 167 (2020), 081504, https://doi.org/10.1149/1945-7111/ab8a97.
- [24] R.K. Gupta, D. Fabijanic, T. Dorin, Y. Qiu, J.T. Wang, N. Birbilis, Simultaneous improvement in the strength and corrosion resistance of Al via high-energy ball milling and Cr alloying, Mater. Des. 84 (2015) 270–276, https://doi.org/10.1016/ i.matdes.2015.06.120.
- [25] J. Esquivel, K.A. Darling, H.A. Murdoch, R.K. Gupta, Corrosion and mechanical properties of Al-5 At. Pet Cr produced by cryomilling and subsequent consolidation at various temperatures, Metall. Mater. Trans. A Phys. Metall. Mater. Sci. 49 (2018) 3058–3065, https://doi.org/10.1007/s11661-018-4620-5.
- [26] J. Esquivel, R.K. Gupta, Corrosion behavior and hardness of Al-M (M: Mo, Si, Ti, Cr) alloys, Acta Metall. Sin. (Engl. Lett. 30 (2017) 333–341, https://doi.org/10.1007/s40195-017-0550-2.
- [27] J. Esquivel, H.A. Murdoch, K.A. Darling, R.K. Gupta, Excellent corrosion resistance and hardness in Al alloys by extended solid solubility and nanocrystalline structure, Mater. Res. Lett. 6 (2018) 79–83, https://doi.org/10.1080/ 21663831.2017.1396262.
- [28] L. Esteves, C.S. Witharamage, J. Christudasjustus, G. Walunj, S.P.O. Brien, S. Ryu, Corrosion behavior of AA5083 produced by high-energy ball milling, J. Alloy. Compd. 857 (2020), 158268, https://doi.org/10.1016/j.jallcom.2020.158268.
- [29] F. Ozdemir, C.S. Witharamage, A.A. Darwish, H. Okuyucu, R.K. Gupta, Corrosion behavior of age hardening aluminum alloys produced by high-energy ball milling, J. Alloy. Compd. 900 (2022), 163488, https://doi.org/10.1016/j. jallcom.2021.163488.

- [30] R.K. Gupta, D. Fabijanic, R. Zhang, N. Birbilis, Corrosion behaviour and hardness of in situ consolidated nanostructured Al and Al-Cr alloys produced via high-energy ball milling, Corros. Sci. 98 (2015) 643–650, https://doi.org/10.1016/j. corsci 2015 06 011
- [31] R.K. Gupta, D. Fabijanic, T. Dorin, Simultaneous improvement in the strength and corrosion resistance of Al via high-energy ball milling and Cr alloying, Mater. Des. 84 (2015) 270–276. https://doi.org/10.1016/J.MATDES.2015.06.120.
- [32] C.S. Witharamage, J. Christudasjustus, J. Smith, W. Gao, R.K. Gupta, Corrosion behavior of an in situ consolidated nanocrystalline Al-V alloy, Npj Mater. Degrad. 6 (2022) 15, https://doi.org/10.1038/s41529-022-00225-5.
- [33] J. Christudasjustus, M.R. Felde, C. Witharamage, J. Esquivel, A.A. Darwish, C. Winker, R.K. Gupta, Age-hardening behavior, corrosion mechanisms, and passive film structure of nanocrystalline Al-V supersaturated solid solution, J. Mater. Sci. Technol. 135 (2023) 1, https://doi.org/10.1016/j.jmst.2022.06.044.
- [34] J. Esquivel, R.K. Gupta, Corrosion Behavior and hardness of Al-M (M: Mo, Si, Ti, Cr) alloys, Acta Metall, Sin. (Engl. Lett. 30 (2017) 333–341.
- [35] C.C. Koch, Structural nanocrystalline materials: an overview, J. Mater. Sci. 42 (2007) 1403–1414, https://doi.org/10.1007/s10853-006-0609-3.
- [36] F. Ozdemir, R.K. Gupta, Influence of vanadium addition on corrosion behavior of high-energy ball milled aluminum alloy 2024, Mater. Corros. (2022) 1–8, https:// doi.org/10.1002/maco.202213478.
- [37] I.K. Wernick, N.J. Themelis, Recycling metals for the envinronment, Annu. Rev. Energy Environ. 23 (1998) 465–497, https://doi.org/10.1146/annurev. energy.23.1.465.
- [38] D. Raabe, D. Ponge, P.J. Uggowitzer, M. Roscher, M. Paolantonio, C. Liu, H. Antrekowitsch, E. Kozeschnik, D. Seidmann, B. Gault, F. De Geuser, A. Deschamps, C. Hutchinson, C. Liu, Z. Li, P. Prangnell, J. Robson, P. Shanthraj, S. Vakili, C. Sinclair, L. Bourgeois, S. Pogatscher, Making sustainable aluminum by recycling scrap: the science of "dirty" alloys, Prog. Mater. Sci. 128 (2022), 100947, https://doi.org/10.1016/j.pmatsci.2022.100947.
- [39] S. Gates-rector, T. Blanton, The powder diffraction file: a quality materials characterization database, Powder Diffr. 34 (2019) 352–360, https://doi.org/ 10.1017/S0885715619000812.
- [40] B.D. Saller, T. Hu, K. Ma, L. Kurmanaeva, E.J. Lavernia, A comparative analysis of solubility, segregation, and phase formation in atomized and cryomilled Al – Fe alloy powders, J. Mater. Sci. 50 (2015) 4683–4697, https://doi.org/10.1007/ s10853-015-9019-8.
- [41] C. Suryanarayana, Mechanical alloying and milling, Prog. Mater. Sci. 46 (2001) 1–184.
- [42] I. Polmear, D. Stjohn, J.-F. Nie, Qian Ma. Light Alloys Metallurgy of the Light Metals. 5th ed., Butterworth-Heinemann, 2017.
- [43] P. Cornette, S. Zanna, A. Seyeux, D. Costa, P. Marcus, The native oxide film on a model aluminium-copper alloy studied by XPS and ToF-SIMS, Corros. Sci. 174 (2020), 108837, https://doi.org/10.1016/j.corsci.2020.108837.
- [44] E.L. Principe, B.A. Shaw, G.D. Davis, Role of oxide / metal interface in corrosion resistance: al-w and al-mo systems, Corrosion 59 (2003) 295–313, https://doi.org/ 10.5006/1.3277562.
- [45] F. Ozdemir, J. Christudasjustus, V.B. Vukkum, R.K. Gupta, Need of an inert atmosphere for high-energy ball milling of Al alloys, J. Mater. Eng. Perform. (2022).
- [46] B.R. Strohmeier, An ESCA Method for Determining the Oxide Thickness on Aluminum Alloys, 15 (1990) 51–56.
- [47] R.K. Gupta, N. Birbilis, The influence of nanocrystalline structure and processing route on corrosion of stainless steel: A review, Corros. Sci. (2014), https://doi.org/ 10.1016/j.corsci.2014.11.041.

- [48] G.S. Frankel, X. Chen, R.K. Gupta, S. Kandasamy, N. Birbilis, Effect of vacuum system base pressure on corrosion resistance of sputtered AI thin films effect of vacuum system base pressure on corrosion resistance of sputtered AI thin films, J. Electrochem. Soc. 161 (2014) C195–C200, https://doi.org/10.1149/ 2.056404jes.
- [49] K.D. Ralston, D. Fabijanic, N. Birbilis, Effect of grain size on corrosion of high purity aluminium, Electrochim. Acta 56 (2011) 1729–1736, https://doi.org/ 10.1016/j.electacta.2010.09.023.
- [50] L. Becker, Chemical elements by market price, (2018). (http://www.leonland.de/elements_by_price/en/list) (accessed June 14, 2022).
- [51] S.K. Das, Emerging trends in aluminum recycling: Reasons and responses, in: TMS Light Met, 2006, 2006, pp. 911–916.
- [52] N. Belov, A. Aksenov, G. Eskin, Iron in Aluminum Alloys Impurity and Alloying Element, Taylor & Francis, London, 2002.
- [53] E.A. Starke, J.T. Staley, Application of modern aluminium alloys to aircraft, Fundam. Alum. Metall. Prod. Process. Appl. 32 (1996) 747–783, https://doi.org/ 10.1533/9780857090256.3.747.
- [54] G. Svenningsen, M.H. Larsen, J.C. Walmsley, J.H. Nordlien, K. Nisancioglu, Effect of artificial aging on intergranular corrosion of extruded AlMgSi alloy with small Cu content, Corros. Sci. 48 (2006) 1528–1543, https://doi.org/10.1016/j. corrol 2005.05.
- [55] R.K. Gupta, A. Deschamps, M.K. Cavanaugh, S.P. Lynch, N. Birbilis, Relating the early evolution of microstructure with the electrochemical response and mechanical performance of a Cu-rich and Cu-Lean 7xxx aluminum alloy, J. Electrochem. Soc. 159 (2012) C492–C502, https://doi.org/10.1149/ 2.062211jes.
- [56] P.M. Natishan, W.E.O. Grady, Chloride ion interactions with oxide-covered aluminum leading to pitting corrosion: a review, J. Electrochem. Soc. 161 (2014) C421–C432, https://doi.org/10.1149/2.1011409jes.
- [57] P.M. Natishan, E. McCafferty, G.K. Hubler, Surface charge considerations in the pitting of ion-implanted aluminum, J. Electrochem. Soc. 135 (1988) 321–327, https://doi.org/10.1149/1.2095608.
- [58] J. Soltis, Passivity breakdown, pit initiation and propagation of pits in metallic materials – review, Corros. Sci. 90 (2015) 5–22, https://doi.org/10.1016/j. corsci.2014.10.006.
- [59] M.A. Meyers, A. Mishra, D.J. Benson, Mechanical properties of nanocrystalline materials, Prog. Mater. Sci. 51 (2006) 427–556, https://doi.org/10.1016/j. pmatsci.2005.08.003.
- [60] Y. Estrin, A. Vinogradov, Extreme grain refinement by severe plastic deformation: a wealth of challenging science, Acta Mater. 61 (2013) 782–817, https://doi.org/ 10.1016/j.actamat.2012.10.038.
- [61] J. Christudasjustus, T. Larimian, J. Esquivel, S. Gupta, A.A. Darwish, T. Borkar, Aluminum alloys with high elastic modulus, Mater. Lett. 320 (2022), 132292, https://doi.org/10.1016/j.matlet.2022.132292.
- [62] J. Christudasjustus, C.S. Witharamage, G. Walunj, T. Borkar, R.K. Gupta, The influence of spark plasma sintering temperatures on the microstructure, hardness, and elastic modulus of the nanocrystalline Al- x V alloys produced by high-energy ball milling, J. Mater. Sci. Technol. 122 (2022) 68–76, https://doi.org/10.1016/j. jmst.2022.02.008.
- [63] K.A. Darling, A.J. Roberts, L. Armstrong, D. Kapoor, M.A. Tschopp, L.J. Kecskes, S. N. Mathaudhu, Influence of Mn solute content on grain size reduction and improved strength in mechanically alloyed Al–Mn alloys, Mater. Sci. Eng. A 589 (2014) 57–65, https://doi.org/10.1016/j.msea.2013.09.047.
- [64] C.S. Witharamage, J. Christudasjustus, R.K. Gupta, The effect of milling time and speed on solid solubility, grain size, and hardness of Al-V alloys, J. Mater. Eng. Perform. (2021) 1–15, https://doi.org/10.1007/s11665-021-05663-x.